



Discontinuous Dynamic Recrystallization Mechanism and Twinning Evolution during Hot Deformation of Incoloy 825

XiTing Zhong, LinKe Huang, and Feng Liu

(Submitted March 4, 2020; in revised form August 24, 2020; published online September 8, 2020)

Discontinuous dynamic recrystallization (DDRX), which involves multiple nucleation and grain growth processes, plays a crucial role in grain refinement; however, the underlying mechanism and the significant role of twin boundaries (TBs) remain poorly understood. Here, the evolution of characteristic microstructures and the fraction and density of TBs under different deformation conditions (i.e., 1050–1200 °C, 0.001–1 s⁻¹) in Incoloy 825 was investigated through a thermomechanical simulator, electron backscattered diffraction (EBSD), and transmission electron microscopy (TEM). The first strand of recrystallized grains nucleated along the original grain boundaries (GBs), separated by the newly formed random high-angle grain boundaries (HAGBs), which were transformed from low-angle grain boundaries (LAGBs) and pre-existing TBs. Subsequently, straight TBs forming in the new grains increased the misorientation angle, promoting the migration of stagnated grain boundaries, and parts of newly generated twinning chains at the front of the recrystallization zone converted into random HAGBs, providing sites for the following layer of nucleation. Moreover, triple junctions between the recrystallized and deformed grains also served as potential nucleation sites when the LAGBs in the large misorientation gradient were transformed into random HAGBs. Quantitative relationships between the recrystallized grain size and TB density were obtained.

Keywords dynamic recrystallization, hot deformation, Incoloy 825, microstructure evolution, twin boundary evolution

1. Introduction

Hot working accompanied by dynamic recrystallization (DRX) is widely used to prepare final or intermediate products in various metals and alloys due to its effective softening and significant control of the microstructure, which improves the formability and mechanical properties of the material (Ref 1-7). Generally, the mechanisms responsible for the formation of multiscale structures can be classified as discontinuous dynamic recrystallization (DDRX) and continuous dynamic recrystallization (CDRX) (Ref 1, 2). For low to medium stacking-fault energy (SFE) alloys that activate dislocation slip and twinning simultaneously (Ref 8, 9), DDRX is the main mechanism during hot deformation and has two obvious steps, i.e., nucleation and grain growth. As the deformed microstructure is replaced by recrystallized grains in an alternating manner of nucleation and grain growth, a typical necklace microstructure

appears, which is a common phenomenon, especially for initially coarse grains. Because of the significant grain refinement that improves the toughness without deterioration of the strength, the necklace mechanism has been a subject of technical importance as well as of scientific interest for decades (Ref 10-15).

Mechanisms regarding the multiple nucleation processes during DDRX have been extensively investigated (Ref 16-25) and generally can be classified into the following types. (1) Nuclei are generated at triple junctions (Ref 16, 17) where stress/strain concentrations and twinning are formed due to inhomogeneous deformation, which makes them the preferred nucleation sites. The following layer of nuclei appears at the triple junctions between the recrystallized and deformed grains (Ref 18) and depends on the GB concavity via the subsequent growth of the first layer of recrystallized grains. (2) The first layer of new grains is nucleated by the bulging of the original GBs, which is assisted by TBs and/or LAGBs at the back of the GB fluctuation (Ref 19, 20). The next layer nuclei form by the local bulging of the GBs between the recrystallized and deformed grains, resulting from high misorientation gradients and coarsening of subgrains (Ref 21). (3) The first necklace is formed by the bulging mechanism as in (2), but the following local expansion does not occur readily because the very high driving force that is essential for offsetting the high surface tension of the bulge is not available in hot deformed microstructures. The subsequent nuclei are produced through the formation of multiple twinning (Ref 22, 23), which is triggered by dislocation interactions in the subgrain boundaries (Ref 24, 25).

For grain growth, it is generally accepted that the GB migration velocity (v) can be expressed by the product of the driving force (P) and its mobility (M) (Ref 26-31), where P is

XiTing Zhong and **LinKe Huang**, State Key Lab of Solidification Processing, Northwestern Polytechnical University, Xi'an 710072 Shaanxi, People's Republic of China; and **Feng Liu**, State Key Lab of Solidification Processing, Northwestern Polytechnical University, Xi'an 710072 Shaanxi, People's Republic of China; and Analytical & Testing Center, Northwestern Polytechnical University, Xi'an 710072 Shaanxi, People's Republic of China. Contact e-mails: hlk@nwpu.edu.cn and liufeng@nwpu.edu.cn.

the free energy difference between adjacent grains that accounts for the stored energy (Ref 26-31), capillary pressure (Ref 27, 28), and solute and/or impurity drag pressure (Ref 28-30); M is strongly dependent on the thermodynamics and crystallography, e.g., the temperature (Ref 26-32) and misorientation of the adjacent grains (Ref 33, 34). For a single-phase material, the stored energy involving deformation defects (e.g., dislocations and subgrains) is always the main factor that drives grain growth (Ref 26-31). However, the effects of TBs on GB migration either are not included or present opposite results in limited studies, i.e., acceleration (Ref 35-38) and obstruction (Ref 39).

In summary, three different types of multiple nucleation mechanisms have been previously proposed for respective conditions, showing that the first recrystallized grains are formed at initial GBs, but the mechanism for the subsequent new grains has not been decided. In addition, the specific TB evolution process (formation and annihilation) during nucleation and grain growth has not been explained clearly. Therefore, a full description of the characterization and mechanism of DDRX and the evolution of twins are still missing in the literature. Therefore, the mechanism behind multiple nucleation and subsequent grain growth processes, accompanied by the effect of TBs, deserves detailed study.

Incoloy 825 is widely used in the chemical and petrochemical industries due to its good mechanical properties and corrosion resistance. It is a medium SFE metallic material with no phase transformations during hot deformation and is an ideal material to characterize the DDRX process, which is mainly controlled by dislocation slip and twinning. Therefore, to investigate the DDRX mechanism and evolution of twins, constant strain rate compression tests through thermomechanical simulation were conducted in a coarse-grained Incoloy 825. Subsequently, the flow stress behavior and microstructure evolution (arrangement and fraction of low-angle grain boundaries (LAGBs), HAGBs and TBs) were investigated to reveal the DDRX mechanism.

2. Materials and Methods

An Incoloy 825 with the chemical composition Fe-40Ni-23.27Cr-3.07Mo-0.67Ti-0.71Mn-1.52Cu (wt.%) was studied here. To prepare a deformation- and defect-free microstructure with a uniform matrix composition and large average grain size, the specimen was solution treated at 1200 °C for 1 h followed by water quenching to room temperature. Isothermal constant strain rate compression tests were carried out on a Gleeble 3500 thermomechanical simulator using cylindrical specimens with a diameter of 8 mm and height of 12 mm. The compression direction was parallel to the cylindrical axis, and tantalum foils were applied between specimens and the platens to minimize friction during deformation. A map of the thermomechanical processing path is shown in Fig. 1, where the deformed sample was heated to 1200 °C at a rate of 30 °C/s, held for 3 min, cooled to the deformation temperature (1050-1200 °C in steps of 50 °C) at a rate of 10 °C/s, and held for 30 s to guarantee that the temperature of the sample was stable and uniform. At the deformation temperature, the samples were compressed to different heights under the strain rate range from 0.001-1 s⁻¹. After deformation, the specimens were water quenched to capture the hot-deformed microstructure. As a comparison, the

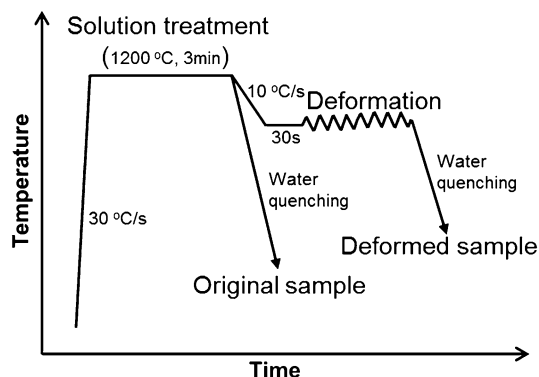


Fig. 1 Schematic diagram of the thermomechanical processing path

original sample was prepared by water quenching after the solution treatment at 1200 °C for 3 min.

Microstructural observation of the original and deformed specimens from the middle part of the axial section was performed via scanning electron microscopy (SEM) equipped with an electron backscattered diffraction (EBSD) detector and transmission electron microscopy (TEM). For the EBSD observations, the samples were electropolished with a solution of 10% perchloric acid in ethanol at 20 V for 30 s at room temperature. The electropolished specimens were observed on an FEI NANO SEM 430 with an operating voltage and a working distance of 20 kV and 15 mm, respectively. The step size ranged from 0.5-4 μm, depending on the average grain size. The TEM examination was performed on an FEI Talos F200X microscope operated at 200 kV, and the specimens were prepared by standard procedures of mechanical grinding from 40–60 μm and ion milling.

Analysis of the EBSD data was performed using HKL channel 5 (Oxford Instruments) software. In the orientation imaging microscopy (OIM) micrographs, three types of boundaries were observed, namely LAGBs with a misorientation angle ($2 < \theta < 15^\circ$), TBs with specific orientation relationships and random HAGBs with a misorientation angle $\theta > 15^\circ$, excluding TBs. Twin boundaries, including primary $\Sigma 3$ ($60^\circ / < 111 >$), and higher order $\Sigma 9$ ($38.94^\circ / < 110 >$), $\Sigma 27a$ ($31.58^\circ / < 110 >$), and $\Sigma 27b$ boundaries ($35.42^\circ / < 210 >$), are presented as red, green, yellow, and yellow lines, respectively. Based on the Brandon criterion of HAGBs (Ref 40), the misorientation tolerance angles of $\Sigma 3$, $\Sigma 9$, and $\Sigma 27$ boundaries were set to 8.66°, 5°, and 2.89°, respectively. Subsequently, the length and number of LAGBs, HAGBs, $\Sigma 3$ boundaries, $\Sigma 9$ boundaries, and $\Sigma 27$ boundaries were counted by using ImageJ (National Institute of Mental Health) software in the grain boundary maps. Furthermore, the recrystallized grains were distinguished from deformed zone by the grain size/shape/orientation and deformation substructure, and the average grain size was measured by the mean linear intercept method in the EBSD data.

3. Results

3.1 Initial Microstructure and Flow Stresses

The initial microstructure, that is, the microstructure of the solution-treated Incoloy 825, is shown in Fig. 2(a) and (b),

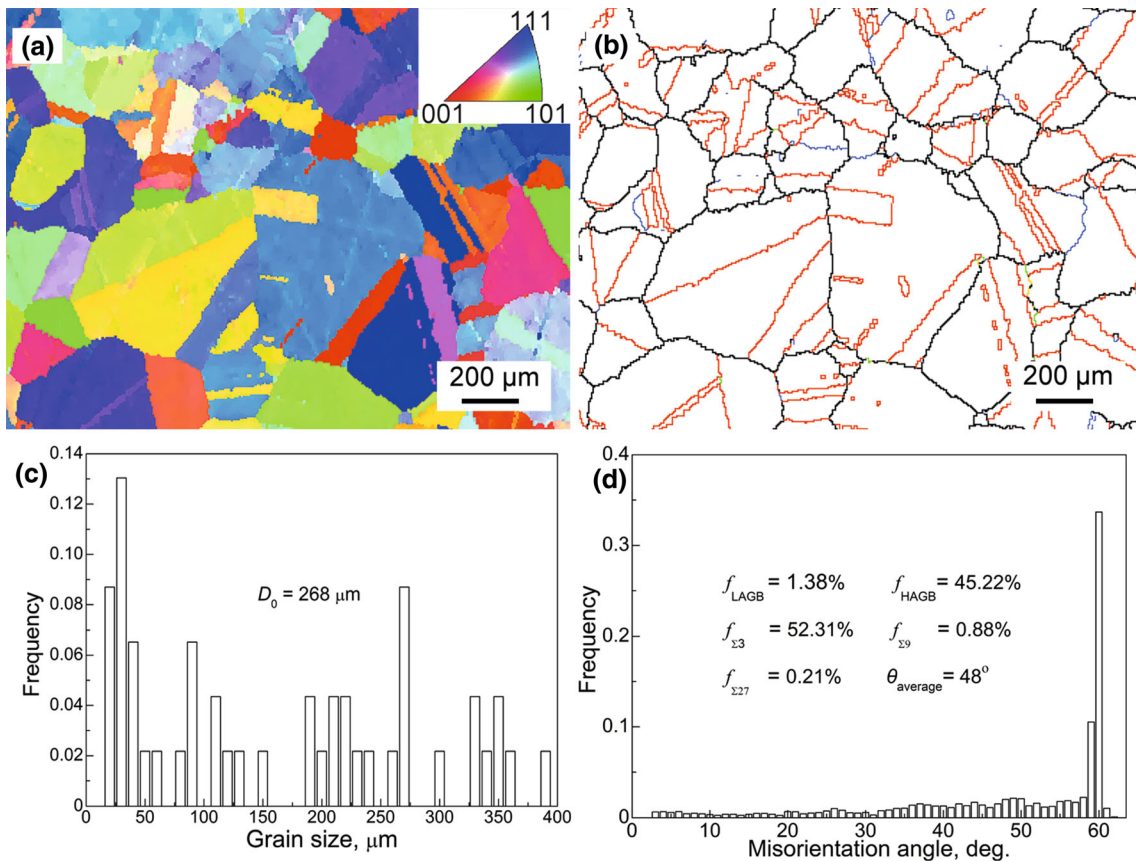


Fig. 2 Microstructures of the initial state: (a) OIM micrograph using a step size of 5 μm , (b) grain boundary map, (c) grain size distribution, and (d) misorientation angle distribution. The thin blue, thick black, thick red, thick green, and thick yellow solid lines represent LAGBs, random HAGBs, $\Sigma 3$ boundaries, $\Sigma 9$ boundaries, and $\Sigma 27$ boundaries, respectively. The colors correspond to the crystallographic orientations indicated in the inverse pole figure (IPF) in (a)

where randomly oriented equiaxed grains with regular and well-defined GBs can be observed. From the grain size and misorientation angle (θ) distribution histogram is shown in Fig. 2(c) and (d), the average grain size (D_0) and θ_{average} are estimated to be 268 μm and 47.7° , respectively. In addition, the length fractions of the LAGBs, random HAGBs, $\Sigma 3$ boundaries, $\Sigma 9$ boundaries, and $\Sigma 27$ boundaries, i.e., the ratio of the specific boundary length to all boundary lengths, are estimated to be 1.38%, 45.22%, 52.31%, 0.88%, and 0.21%, respectively, as displayed in Fig. 2(d). As shown, there is a high fraction of TBs, which is consistent with the grain boundary map in Fig. 2(b), where the TBs were distributed in and penetrated almost all grains. Note that the TBs are almost all $\Sigma 3$ boundaries, and $\Sigma 9$ and $\Sigma 27$ boundaries are rare.

Figure 3 shows the true stress–true strain (σ – ϵ) curves under different thermomechanical conditions, where the deformation temperature (T) ranges from 1050 to 1200 $^\circ\text{C}$ and the strain rate ($\dot{\epsilon}$) ranges from 0.001 to 1 s^{-1} . Generally, the flow stress first increases to a maximum value (peak stress, σ_p) and then decreases to an almost constant true stress (the steady-state stress, σ_s). In Fig. 3(a), it is shown that for a fixed deformation strain rate (i.e., 0.01 s^{-1}), the decreased deformation temperature tends to increase both σ_p and σ_s . Similarly, for a constant deformation temperature (i.e., 1150 $^\circ\text{C}$), both σ_p and σ_s increase with increasing strain rate from 0.001 to 1 s^{-1} , while a peak stress is obtained at 1 s^{-1} , as shown in Fig. 3(b). In summary, the overall level, distinct peak, and steady-state

stresses increase with decreasing T and increasing $\dot{\epsilon}$, attesting to the typical characteristics of DDRX flow (Ref 1, 2, 6, 38).

3.2 Evolution of the Deformed Microstructure

To explore the DDRX mechanism, hot deformation at different temperatures and $\dot{\epsilon} = 0.01 \text{ s}^{-1}$ are interrupted at a certain strain (e.g., 0.916), and then the deformed samples are quenched to room temperature for characterization, as shown in Fig. 4. Different degrees of DDRX occur during different deformation conditions, and with decreasing T , the recrystallized area and average D_{DDRX} decrease. In addition, straight TBs and TB clusters are observed in the recrystallized grains but absent in the deformed grains. The D_{DDRX} corresponding to $T = 1050 \text{ }^\circ\text{C}$ (Fig. 4d2) is much smaller than the initial grain size of the solution-treated sample (Fig. 2c), implying multiple nucleation and grain growth processes; the nuclei of the next/following layer are shown in Fig. 4(d1), where the new grains are almost all formed at triple junctions. In addition, the characterized substructures in the deformed grains are LAGBs at high temperatures of 1200 and 1150 $^\circ\text{C}$, well-developed equiaxed subgrains at 1100 $^\circ\text{C}$, and elongated subgrains at 1050 $^\circ\text{C}$. Correspondingly, the LAGB frequencies increase sharply with decreasing T , in addition to the more stable TBs frequencies, resulting in a decrease in the average misorientation angle (θ_{average}), as illustrated by the misorientation angle distribution in Fig. 4.

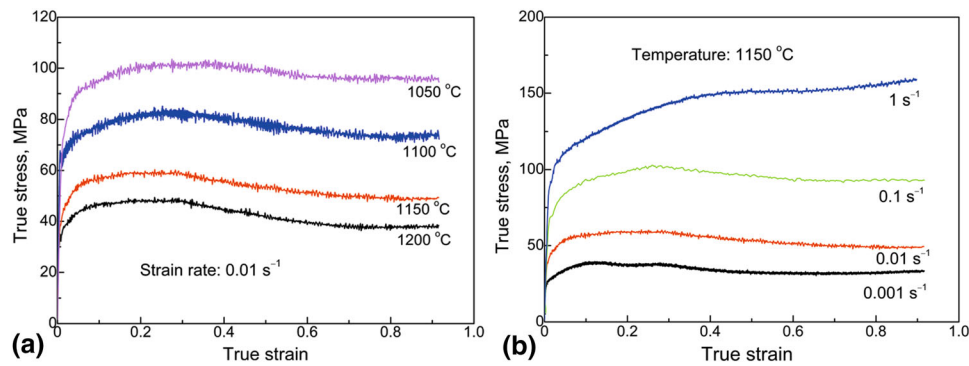


Fig. 3 True stress–true strain curves under different deformation conditions: (a) different T at $\dot{\epsilon} = 0.01 \text{ s}^{-1}$ and (b) different $\dot{\epsilon}$ at $T = 1150 \text{ }^\circ\text{C}$

Moreover, the evolution of the microstructure, D_{DDRX} , and θ distribution under different $\dot{\epsilon}$ is similar to that under different T , e.g., the recrystallized area, average D_{DDRX} , and θ_{average} decrease with increasing $\dot{\epsilon}$, as shown in Fig. 5. In addition, the substructures in deformed grains change from a few LAGBs to elongated subgrains and parallel microbands (MBs) with increasing $\dot{\epsilon}$, as shown in the grain boundary maps in Fig. 5. At high $\dot{\epsilon}$ (1 s^{-1}), the necklace microstructure is produced, and new grains are generated at the triple junctions between the original and recrystallized grains (indicated by the arrows in Fig. 5d1). Simultaneously, LAGBs and the pre-existing TBs are gradually transformed into new random HAGBs, resulting in discontinuous HAGBs and TBs in the deformed grains (indicated by the arrows in Fig. 5d1).

Specific microstructures under different strains at $T = 1100 \text{ }^\circ\text{C}$ and $\dot{\epsilon} = 0.01 \text{ s}^{-1}$ are presented in Fig. 6, where multiple nucleation and grain growth processes during DDRX are revealed. At low strains (e.g., 0.22), the original GB fluctuates due to the strain-induced grain boundary migration (SIBM), and the first layer of recrystallized grains forms by the GB bulging mechanism and is assisted by pre-existing TBs and subboundaries (arrows in Fig. 6a1), resulting in the typical necklace microstructure, as shown in Fig. 6(a1). An increase in the strain (0.51) gives rise to the appearance of a second nucleation layer between the recrystallized and deformed grains and the development of plentiful subgrains in the deformed grains. Upon further deformation ($\epsilon = 1.39$ in Fig. 6d1), the deformed microstructures are completely replaced by recrystallized structures with slight grain growth. Simultaneously, the distribution range of D_{DRX} broadens, and the average value increases as ϵ increases, consistent with the development of nucleation and grain growth. Similarly, θ_{average} increases with the DDRX process, resulting from the increased HAGB frequency, the decreased LAGB frequency, and the more stable TB frequency, as presented in Fig. 6.

The evolution of the recrystallized fraction (f_{DDRX}) and D_{DDRX} and the quantification of specific boundaries (i.e., HAGBs, LAGBs, and TBs, including $\Sigma 3$, $\Sigma 9$, and $\Sigma 27$ boundaries, which are presented in Fig. 4, 5, and 6, are displayed in Fig. 7. Generally, with decreasing T and increasing $\dot{\epsilon}$, f_{DDRX} , D_{DDRX} , f_{HAGB} , and f_{TB} decrease, while f_{LAGB} increases, consistent with the microstructural evolution in Fig. 4, 5, and 6. As shown in Fig. 7(e) and (f), however, with increasing ϵ , f_{HAGB} and f_{TB} decrease first and then increase, while f_{LAGB} increases and then decreases rapidly. At the early deformation stage, a large number of dislocation substructures form in the original grains, accompanied by the gradual

disappearance of pre-existing TBs. Hence, as the deformation continues, f_{LAGB} increases sharply, and f_{TB} and f_{HAGB} decrease. Subsequently, deformation defects are consumed due to the generation and growth of recrystallized grains, and TBs are formed at the same time, resulting in increased f_{TB} and f_{HAGB} and decreased f_{LAGB} .

3.3 Characteristic Microstructures

Based on the microstructural evolution during different deformation conditions in Sect. 3.2, dislocation substructures and twin boundaries play a significant role in nucleation and grain growth. With decreasing T and/or increasing $\dot{\epsilon}$, dislocation substructures vary from few LAGBs to well-developed equiaxed, elongated subgrains and microbands. Moreover, pre-existing TBs in deformed grains are annihilated, and new TBs form in recrystallized grains as DDRX progresses. Hence, the specific dislocation substructures and TBs under different deformation conditions are shown in Fig. 8, 9, and 10.

Typical substructures and the corresponding θ variation at $T = 1100 \text{ }^\circ\text{C}$ and $\dot{\epsilon} = 0.01 \text{ s}^{-1}$ are presented in Fig. 8(a1)–(b3), showing the substructural evolution during DDRX. At small strains (0.22), dislocation cells/subgrains form near the original GBs, as verified by the point-to-point (local) and point-to-origin (cumulative) misorientation angle versus distance of line A1 (Fig. 8a2), where platforms of cumulative θ ($> 2^\circ$) are produced. In addition, obvious initial GB bulging appears due to the strong SIBM, which is manifested by the trend of local and cumulative θ along line A2 in Fig. 8(a3). When $\epsilon = 0.51$ (Fig. 8b1–b3), larger θ plateaus are formed along lines B1 and B2, in which the cumulative θ is more than 5° with a small local θ ($< 2^\circ$), and the step widths are approximately $15 \mu\text{m}$ and $20 \mu\text{m}$, respectively, indicating that well-developed subgrains are generated inside the deformed grains. The specific substructures and θ versus distance at $T = 1150 \text{ }^\circ\text{C}$, $\dot{\epsilon} = 1 \text{ s}^{-1}$, and $\epsilon = 0.916$, are displayed in Fig. 8(c1)–(c3), where elongated subgrains and even parallel microbands are observed. The cumulative θ parallel (line C1) and vertical to GB (line C2) stepwise increase to 30° and 45° , respectively, where the plateau spaces are approximately $15 \mu\text{m}$, and the local θ ($> 5^\circ$) between plateaus implies the existence of developing LAGBs.

In addition, the annihilation and formation of TBs are also observed in the hot deformed microstructure. To investigate the evolution of TBs and the association with DDRX, typical patterns of TBs are analyzed in Fig. 9. Based on the OIM graph in Fig. 9a1 and the variation of θ along line D1 (Fig. 9a2),

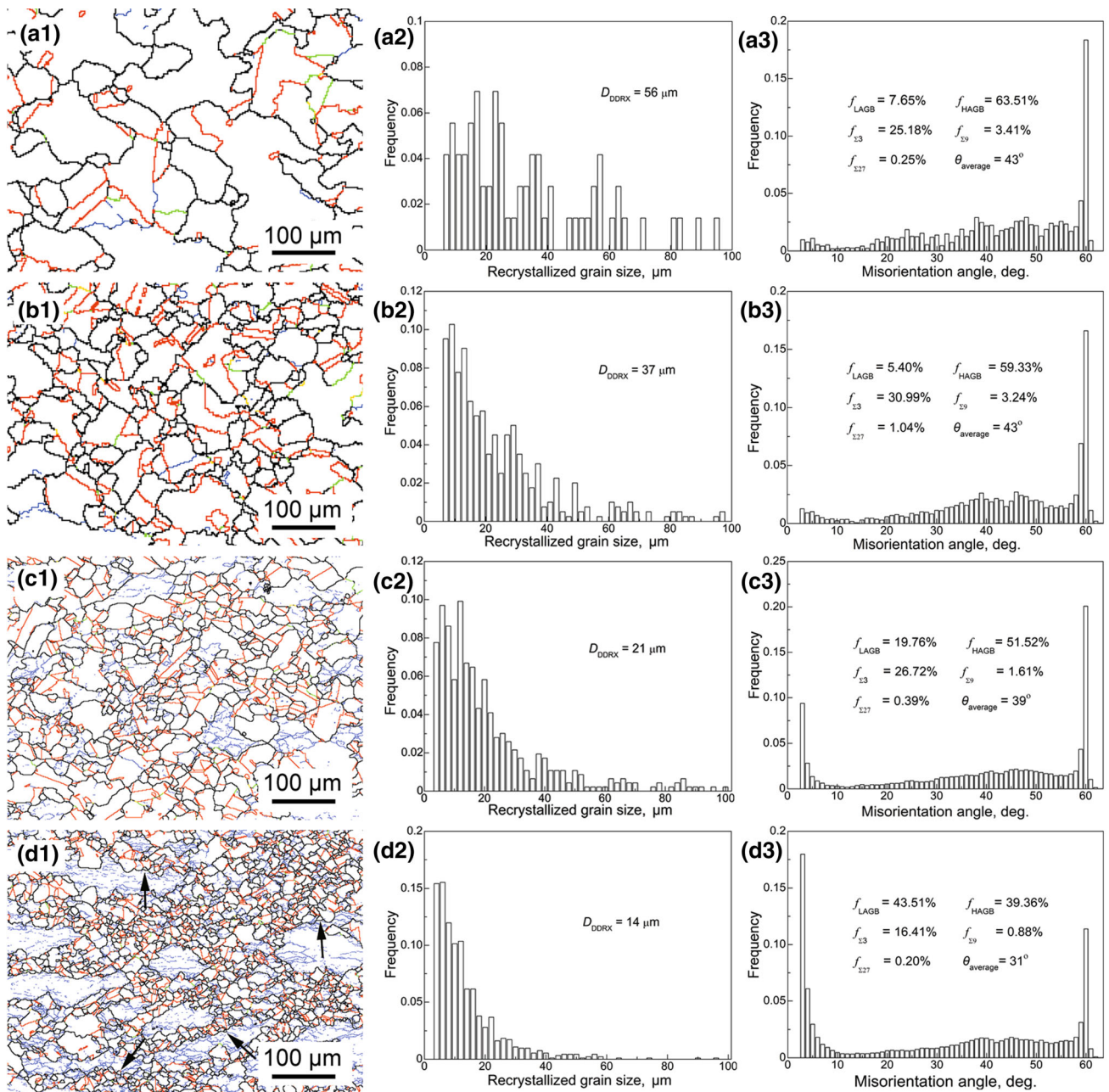


Fig. 4 Grain boundary maps, recrystallized grain size distributions and misorientation angle distributions of Incoloy 825 hot deformed to a true strain of 0.916 at a $\dot{\epsilon}$ of 0.01 s^{-1} under different T : (a1, a2, a3) 1200 °C, (b1, b2, b3) 1150 °C, (c1, c2, c3) 1100 °C, and (d1, d2, d3) 1050 °C. The step sizes of the grain boundary maps in (a1, b1, c1, and d1) are 2, 2, 1, and 1 μm , respectively. The line styles in the grain boundary maps have the same definitions as those in Fig. 2(b)

substantial dislocation subboundaries pileup near the pre-existing TBs, leading to the TBs deviating from the twinning relationship (the specific misorientation angles are presented in Fig. 9a1). Subsequently, the straight pre-existing TBs bend and then partially transform into random HAGBs, which convert completely with increasing strain. On this basis, recrystallized grains appear along the transforming pre-existing TB assisted by the LAGBs and first form at triple junctions and near the original GB bulging (Fig. 6a1), for example, grains 2, 3, 5, and 6 in Fig. 9(a1) and (b1). Furthermore, during the growth of the nuclei, recrystallized grains are divided into new and old parts, owing to the formation of new straight TBs inside, as shown in Fig. 9(a1) and (b1). According to the θ change across the

deformed (grains 1 and 4), new (grains 2 and 5), and old (grains 3 and 6) recrystallized grains, i.e., lines D2 and D1, the $\Delta\theta$ between the recrystallized and deformed grains are accumulated from 37° to 52° (Fig. 9a3) and from 29° to 47° (Fig. 9b2), respectively, promoting the further migration of recrystallized GBs into deformed grains (Ref 33, 34). Except for the straight TBs formed in the recrystallized grains, clusters of newly formed TBs are observed at the front of the recrystallized grains (Fig. 9c1), consisting mostly of $\Sigma 3$ boundaries and a few $\Sigma 9$ and $\Sigma 27$ boundaries. Subsequently, parts of new TBs transform into random HAGBs similar to the behavior as shown in Fig. 9(a1), and new grains are generated in the twinning chains,

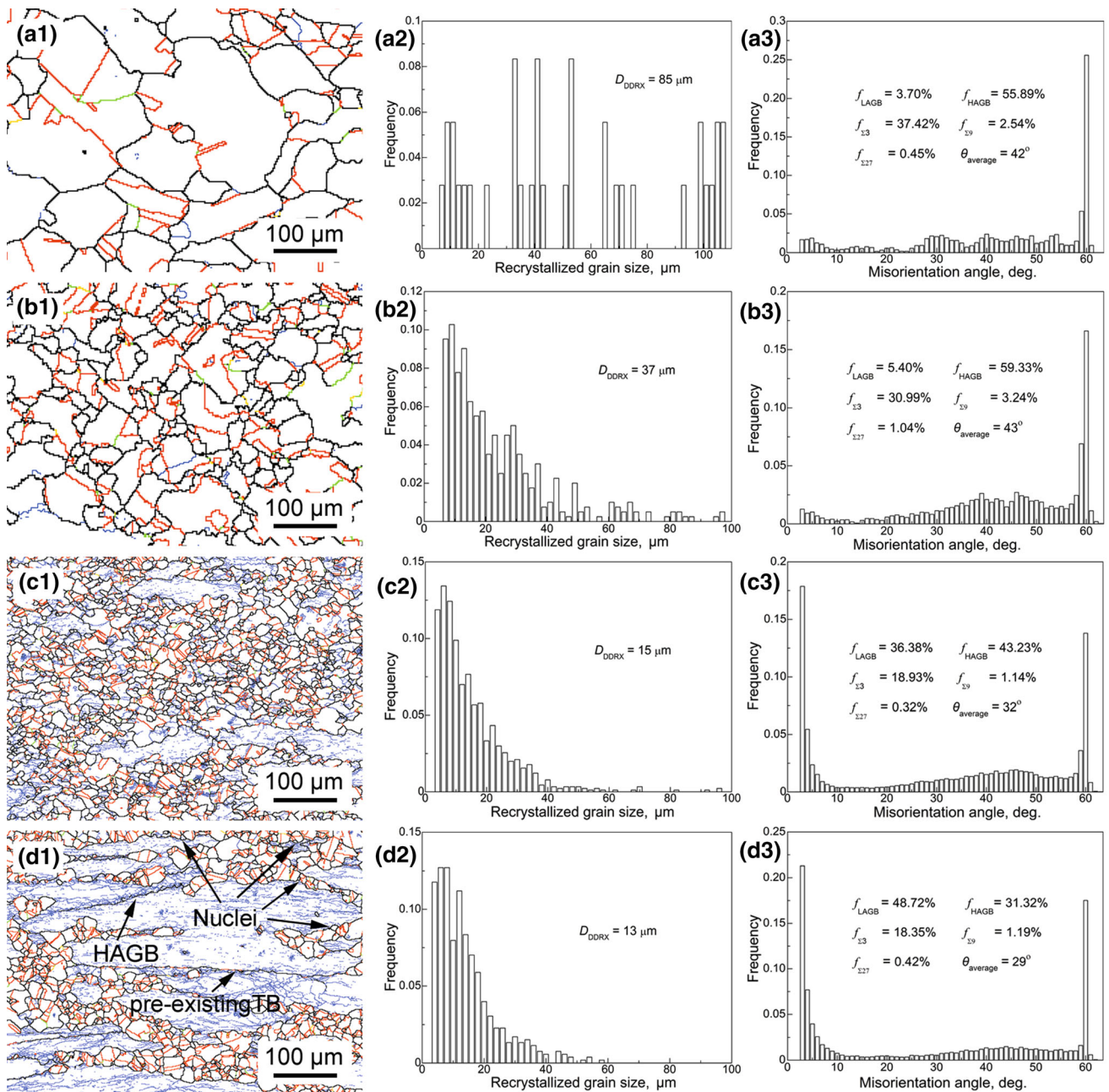


Fig. 5 Grain boundary maps, recrystallized grain size distributions and misorientation angle distributions of Incoloy 825 hot deformed to a true strain of 0.916 at $T = 1150\text{ }^{\circ}\text{C}$ under different $\dot{\epsilon}$: (a1, a2, a3) 0.001 s^{-1} , (b1, b2, b3) 0.01 s^{-1} , (c1, c2, c3) 0.1 s^{-1} , and (d1, d2, d3) 1 s^{-1} . The step sizes of the grain boundary maps in Fig. a1, b1, c1, and d1 are 2, 2, 1, and 1 μm , respectively. The line styles in the grain boundary maps have the same definitions as those in Fig. 2(b)

as shown in Fig. 9(c2), supplying another mechanism for nucleation on the next layer.

The TEM micrographs of characteristic substructures under different deformation conditions are presented in Fig. 10. At the early stage of DDRX, a high density of dislocations tangle to form LAGBs and then subgrains (Fig. 10a) where the low-energy substructures are developing, which is consistent with the plateaus with low cumulative θ values in Fig. 8(a1)-(a3). As

the strain increases, well-developed subgrains are formed in deformed grains (Fig. 10b), corresponding to the large θ ($> 5^{\circ}$) plateaus in Fig. 8(b1)-(b3). In addition, parallel microbands under deformation at $T = 1150\text{ }^{\circ}\text{C}$, $\dot{\epsilon} = 1\text{ s}^{-1}$ and $\epsilon = 0.916$ are presented in Fig. 10(c), which is verified by the stepwise increased cumulative θ variation (Fig. 8c1-c3). The selected area electron diffraction (SAED) with two sets of identical diffraction spots in Fig. 10(d) indicates the occurrence of TBs in recrystallized grains.

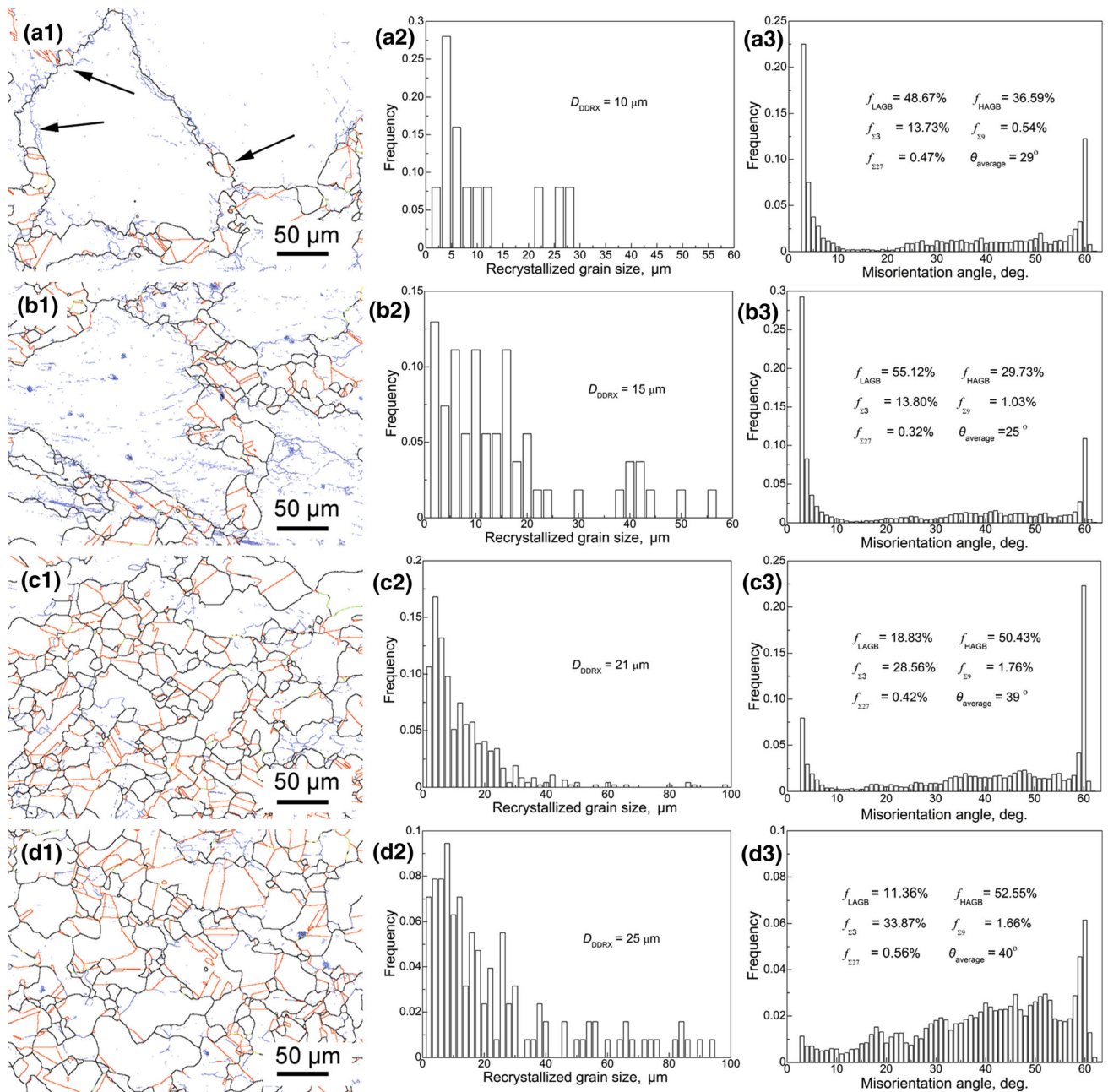


Fig. 6 Grain boundary maps, recrystallized grain size distributions and misorientation angle distributions of Incoloy 825 hot deformed at $T = 1100\text{ }^{\circ}\text{C}$ and $\dot{\epsilon} = 0.01\text{ s}^{-1}$ to different strains: (a1, a2, a3) 0.22, (b1, b2, b3) 0.51, (c1, c2, c3) 0.916, and (d1, d2, d3) 1.39. The step sizes of the grain boundary maps in this figure are all $0.5\text{ }\mu\text{m}$. The line styles in the grain boundary maps have the same definitions as those in Fig. 2(b)

4. Discussion

4.1 Recrystallization Mechanism

Based on the experimentally observed microstructural evolution in the Incoloy 825 under different deformation conditions (Fig. 4, 5, 6, 7, 8, 9, and 10), we present a mechanism for DDRX, as schematically presented in Fig. 11, where a schematic of nucleation, grain growth, and TB evolution are also displayed. After the solution treatment of Incoloy 825 (Fig. 2), a high density of TBs is observed to be distributed in the original grains, as shown in Fig. 11a-I. In the early deformation stage, numerous dislocations accumulate

near the initial GBs to produce a large number of subboundaries and bulging GBs (Fig. 8a1). Moreover, the TBs are barriers to dislocation slip so that abundant LAGBs pileup at the pre-existing TBs (Ref 41). Then, the pre-existing straight TBs bend and deviate from the twinning orientation, finally forming a random HAGB orientation with deformation (Fig. 9a1). Therefore, the preferred recrystallized grains first appear at the triple junctions (Fig. 11a-II), and then the necklace structure forms along the initial GB (Fig. 11a-III), with the assistance of developing LAGB and transforming pre-existing TB (Fig. 11b and d), which is consistent with the experimental results in Fig. 6(a1) and 8(a1).

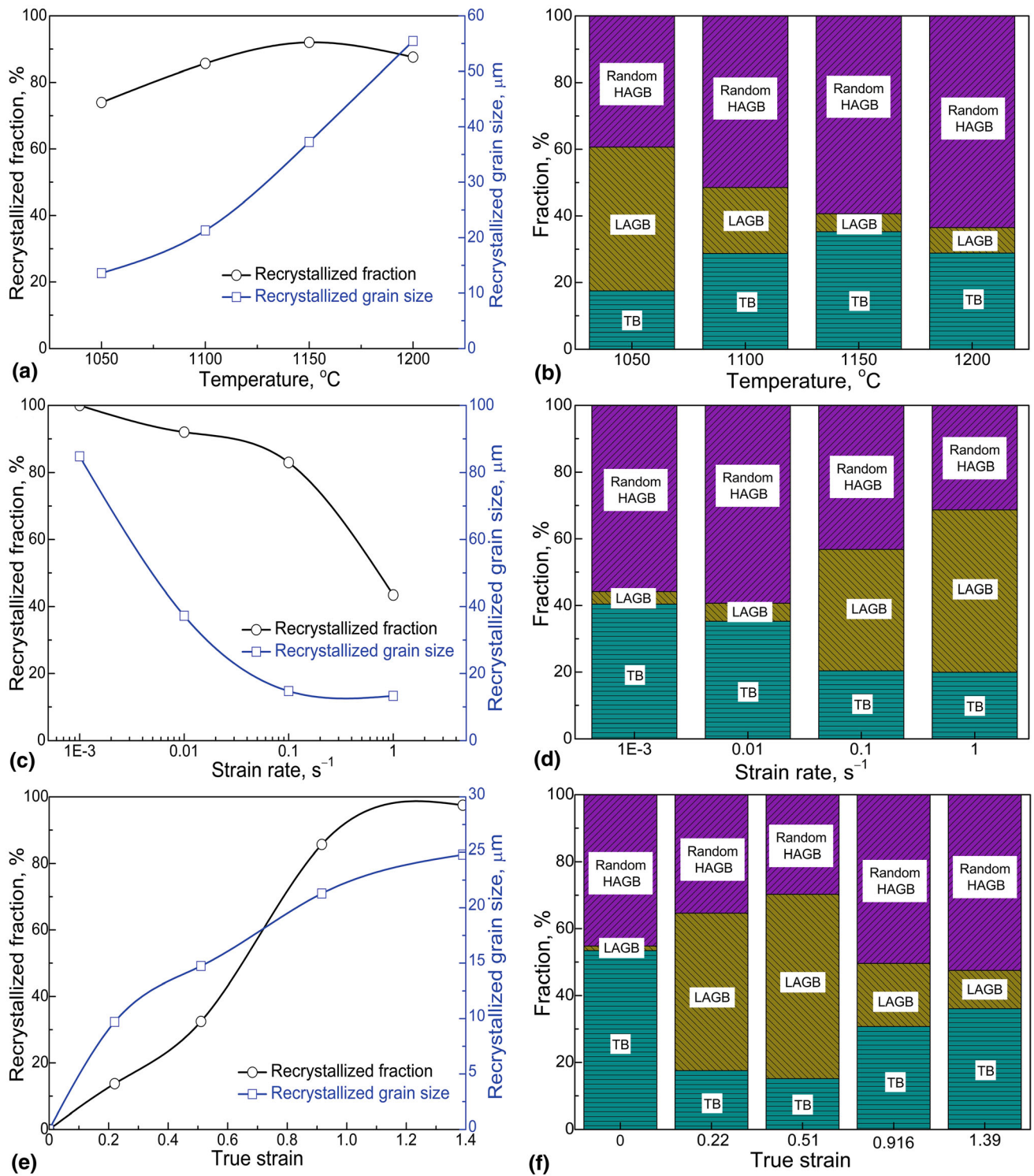


Fig. 7 Evolution of recrystallized fraction (f_{DDRX}), average recrystallized grain size (D_{DDRX}), HAGB fraction (f_{HAGB}), LAGB fraction (f_{LAGB}), and TB (which includes primary twin $\Sigma 3$ and higher order twins $\Sigma 9$ and $\Sigma 27$) fraction (f_{TB}), under different deformation conditions: (a) different T at $\dot{\epsilon} = 0.01 \text{ s}^{-1}$ and $\epsilon = 0.916$; (b) different $\dot{\epsilon}$ at $T = 1150 \text{ }^{\circ}\text{C}$ and $\epsilon = 0.916$, and (c) different ϵ at $T = 1100 \text{ }^{\circ}\text{C}$ and $\dot{\epsilon} = 0.01 \text{ s}^{-1}$

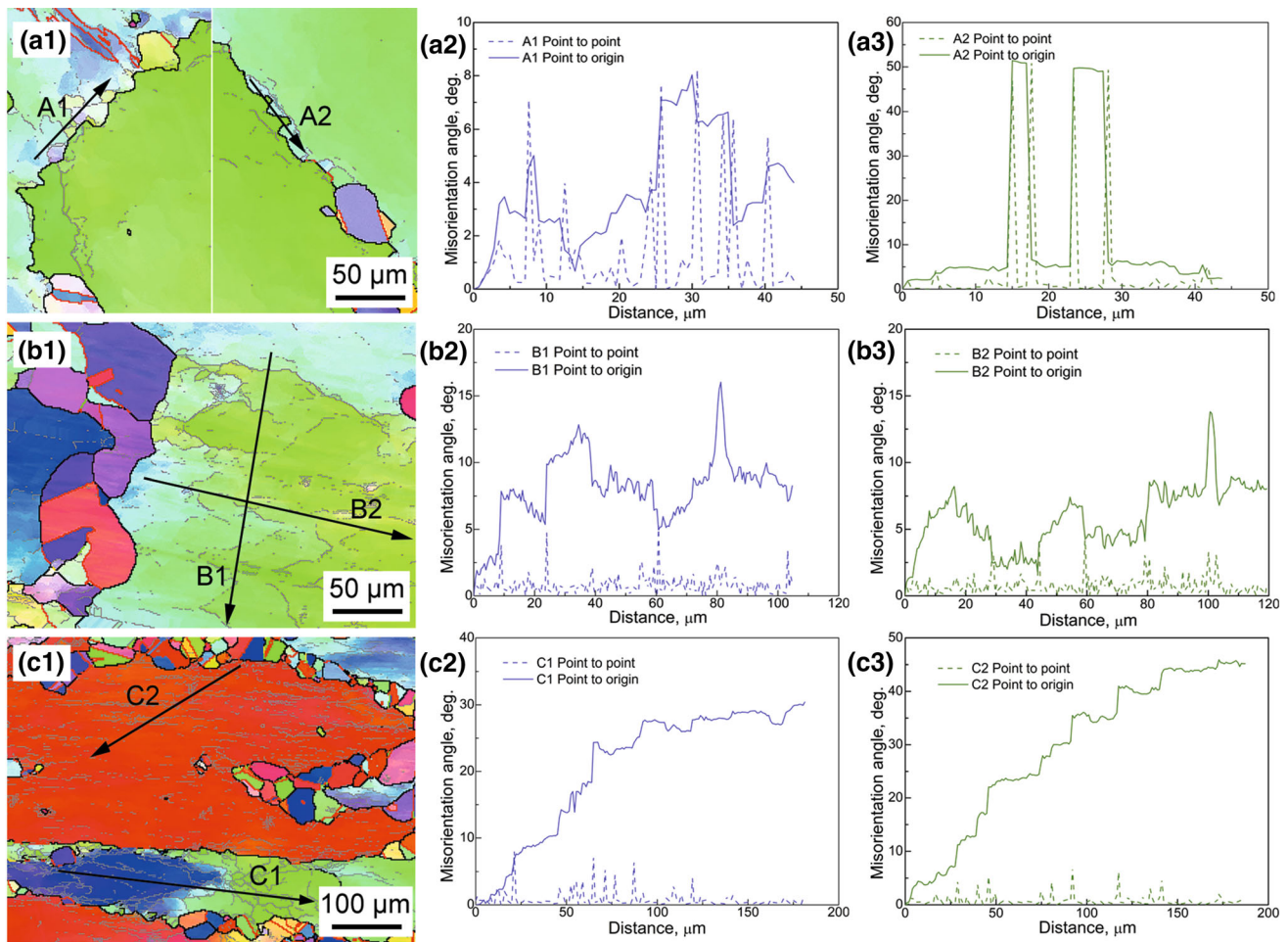


Fig. 8 OIM maps and orientation analysis for specific substructures under different deformation conditions: (a1, a2, a3) $T = 1150\text{ }^{\circ}\text{C}$, $\dot{\epsilon} = 0.01\text{ s}^{-1}$, and $\epsilon = 0.22$; (b1, b2, b3) $T = 1100\text{ }^{\circ}\text{C}$, $\dot{\epsilon} = 0.01\text{ s}^{-1}$, and $\epsilon = 0.51$; and (c1, c2, c3) $T = 1150\text{ }^{\circ}\text{C}$, $\dot{\epsilon} = 1\text{ s}^{-1}$, and $\epsilon = 0.916$. Thin gray, thick black, thick red, thick green, and thick yellow solid lines represent LAGBs, random HAGBs, $\Sigma 3$ boundaries, $\Sigma 9$ boundaries, and $\Sigma 27$ boundaries, respectively. The colors in the OIM micrographs have the same definitions as those in Fig. 2(a)

Furthermore, the grain growth stagnates due to the consumed stored energy and similar orientation between the recrystallized and deformed grains. Therefore, new straight TBs are produced by a “growth accident” (Ref 25) in recrystallized grains to increase the driving force for GB migration (Fig. 9a1 and b1) (Ref 32), which promotes the consumption of deformed microstructure. Upon further deformation, mature subgrains (Fig. 8b1) and microbands are formed (Fig. 8c1) in the deformed grains, resulting in a large misorientation gradient and discontinuous random HAGBs, as shown in Fig. 5(d1), which promote subsequent nucleation at triple junctions. Moreover, one elongated deformed grain is divided into several grains due to the transformation of the pre-existing TBs inside completely into random HAGBs (Fig. 5d1). In addition, as presented in Fig. 9(c1) and (c2), at the front of the recrystallized grains, clustered TBs emerge, some of which transform into random HAGBs upon further deformation (Fig. 11d), subsequently promoting nucleation and grain growth (Ref 36). Therefore, the next layer of recrystallized grains is accomplished by the twinning chains and the addition of triple junctions supplied by the first small new grains, concurrent with the highly developed substructures, as presented in

Fig. 11a-IV. In summary, the DDRX of the original deformed grains occurs by multiple nucleation and grain growth processes, where the first layer of recrystallized grains is generated along the original GBs, and there are two main nucleation mechanisms for the following layer of nuclei, i.e., parts of the twinning chains at the front of the new grains and highly developed LAGBs in the large misorientation gradient transform into random HAGBs.

4.2 Twinning Evolution

Figure 7 shows the evolution of f_{TB} as a function of T , $\dot{\epsilon}$ and ϵ , which strongly depends on other boundaries, especially for the large number of LAGBs at the early stage DDRX. As displayed in Fig. 12(a)-(d), the average number and length of TBs (including $\Sigma 3$, $\Sigma 9$, and $\Sigma 27$ boundaries) per total/recrystallized area, ρ_L and ρ_N both in total and recrystallized regions increase with an decrease in T and increase in $\dot{\epsilon}$, excluding the TB density in the total area (Fig. 12c) at $\dot{\epsilon} = 1\text{ s}^{-1}$. At a high strain rate ($\dot{\epsilon} = 1\text{ s}^{-1}$), a small number and length of newly generated TBs are produced due to the small recrystallized area, in addition to the negligible pre-existing

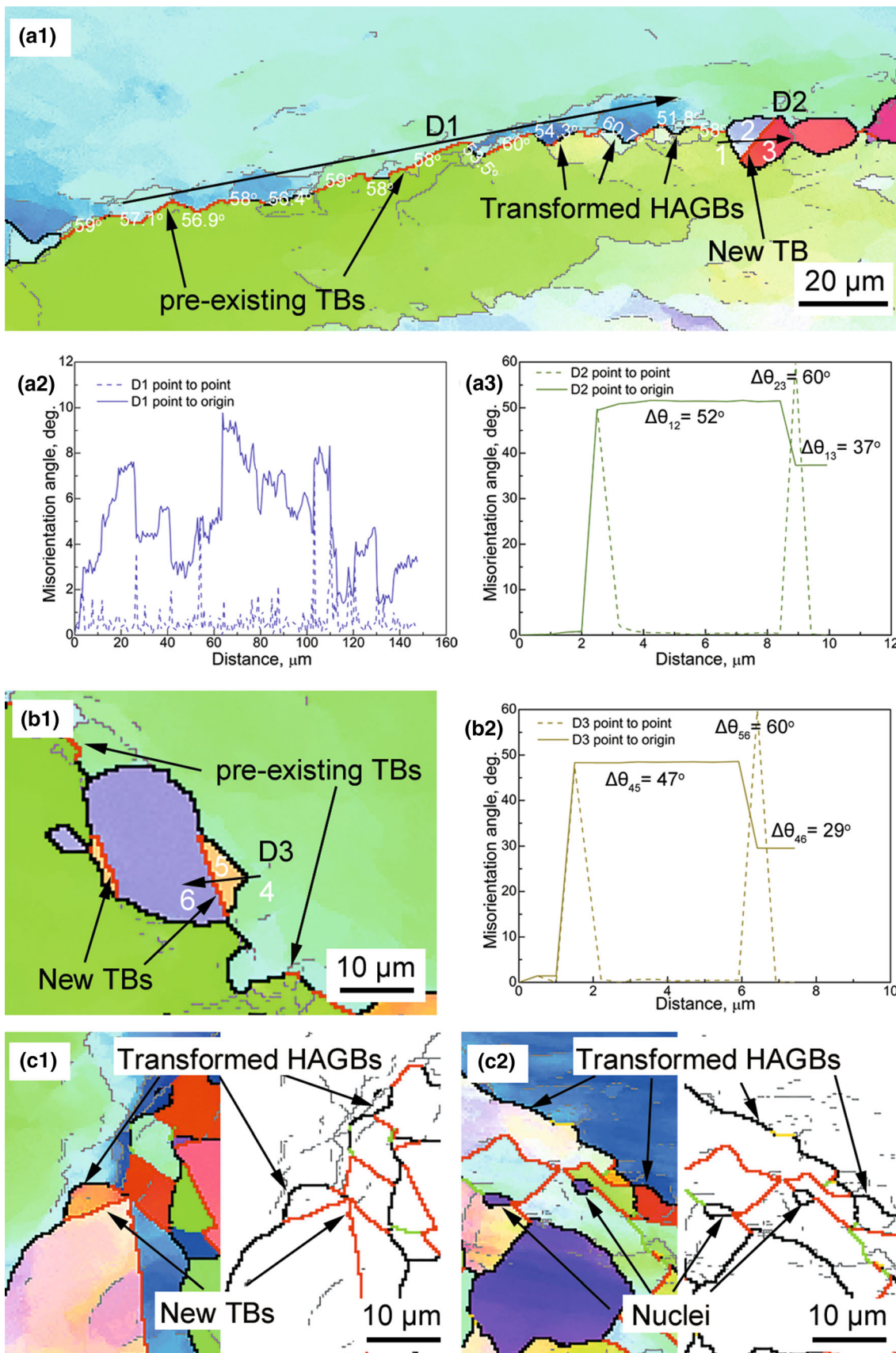


Fig. 9 OIM maps and orientation analysis for TBs under different deformation conditions, (a1, a2, a3) $T = 1100\text{ }^{\circ}\text{C}$, $\dot{\epsilon} = 0.01\text{ s}^{-1}$, $\epsilon = 0.16$; (b1, b2, c1) $T = 1100\text{ }^{\circ}\text{C}$, $\dot{\epsilon} = 0.01\text{ s}^{-1}$, $\epsilon = 0.22$; (c2) $T = 1100\text{ }^{\circ}\text{C}$, $\dot{\epsilon} = 0.01\text{ s}^{-1}$, $\epsilon = 0.51$. The step sizes of the grain boundary maps in this figure are all $0.5\text{ }\mu\text{m}$. The colors and line styles in the OIM micrographs have the same definitions as those in Fig. 8

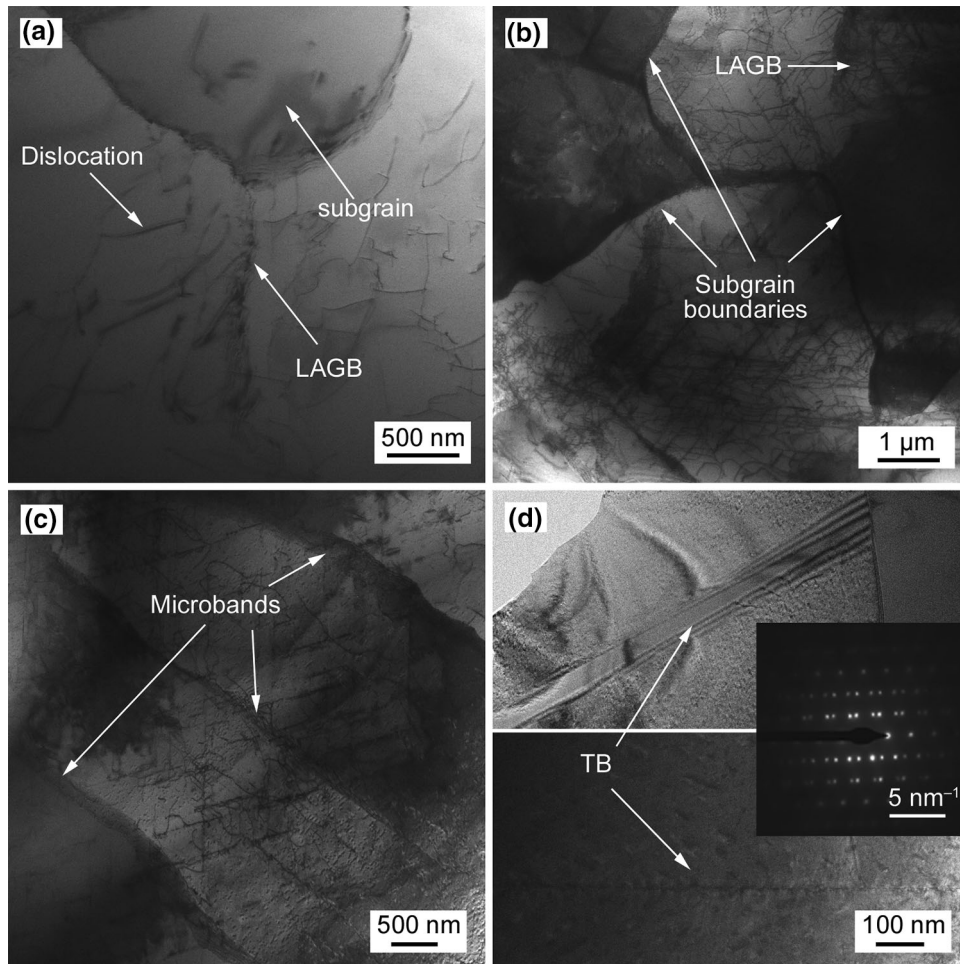


Fig. 10 TEM micrographs of characteristic substructures under different deformation conditions: (a) $T = 1100\text{ }^{\circ}\text{C}$, $\dot{\varepsilon} = 0.01\text{ s}^{-1}$, and $\varepsilon = 0.22$; (b) $T = 1100\text{ }^{\circ}\text{C}$, $\dot{\varepsilon} = 0.01\text{ s}^{-1}$, and $\varepsilon = 0.51$; (c) $T = 1150\text{ }^{\circ}\text{C}$, $\dot{\varepsilon} = 1\text{ s}^{-1}$, and $\varepsilon = 0.916$; and (d) $T = 1100\text{ }^{\circ}\text{C}$, $\dot{\varepsilon} = 0.01\text{ s}^{-1}$, and $\varepsilon = 0.916$

TBs; therefore, ρ_L and ρ_N in the total area are lower than that of $\dot{\varepsilon} = 0.1\text{ s}^{-1}$, showing a peak in Fig. 12(c). The quantitative change in TB densities with increasing ε is shown in Fig. 12(e) and (f), where ρ_L and ρ_N are increased in the total area and decreased in the recrystallized area with decreasing amplitude.

Based on the above analysis (Sect. 4.1), the pre-existing TBs in the original grains are gradually transformed into random HAGBs to assist the first layer of nucleation, dividing a deformed grain into several parts. Due to the “growth accident” (Ref 25) and “regeneration mechanism” (Ref 35, 42), new TBs are formed in the recrystallized grains and at the front of recrystallization, which then promotes GB migration into deformed microstructures and subsequent layer nucleation. On this basis, TBs consisting of twinning chains are believed to promote nucleation, whereas linear TBs are considered to facilitate grain growth, which suggests that additional TBs are required when nucleation is stimulated while growth is hindered. Following previous studies (Ref 43, 44), nucleation is enhanced and grain growth is weakened with decreasing T and increasing $\dot{\varepsilon}$, which then increases the TB densities (ρ_L , ρ_N) both in the total and recrystallized regions, consistent with the current experimental results shown in Fig. 12(a)-(d). On the other hand, the TB densities (ρ_L , ρ_N) in the total and

recrystallized areas with increasing ε illustrate an opposite trend, as presented in Fig. 12(e) and (f). In view of the twinning evolution in Fig. 11, TBs form during hot deformation to promote subsequent GB migration and nucleation, while they are annihilated due to GB migration in the recrystallized zone to decrease the systematic interfacial energy (Ref 35); therefore, the TB densities (ρ_L , ρ_N) in the total area increase with increasing ε and decrease at the end of DDRX (Fig. 12e). Note that the conversion of TBs into random HAGBs is required for the nucleation of the following layer, and the partial annihilation of twinning chains is considered the TB content of the previous recrystallized zone. Therefore, the TB densities (ρ_L , ρ_N) increase in the total area and decrease in the recrystallized area with increasing ε , as presented in Fig. 12(f).

Furthermore, the variation in the TB densities is dependent on the DDRX process (i.e., nucleation and grain growth), thus changing f_{DRX} and D_{DDRX} . Pande et al. (Ref 45) suggested that the twin density is determined uniquely by the grain size. Then, upon plotting and fitting the relationships between the TB densities in the recrystallized area and D_{DDRX} , it is clear from Fig. 13 that ρ_L and ρ_N decrease with the increased D_{DDRX} , in good agreement with previous research results (Ref 46-48). These typical relationships are well fitted with power functions

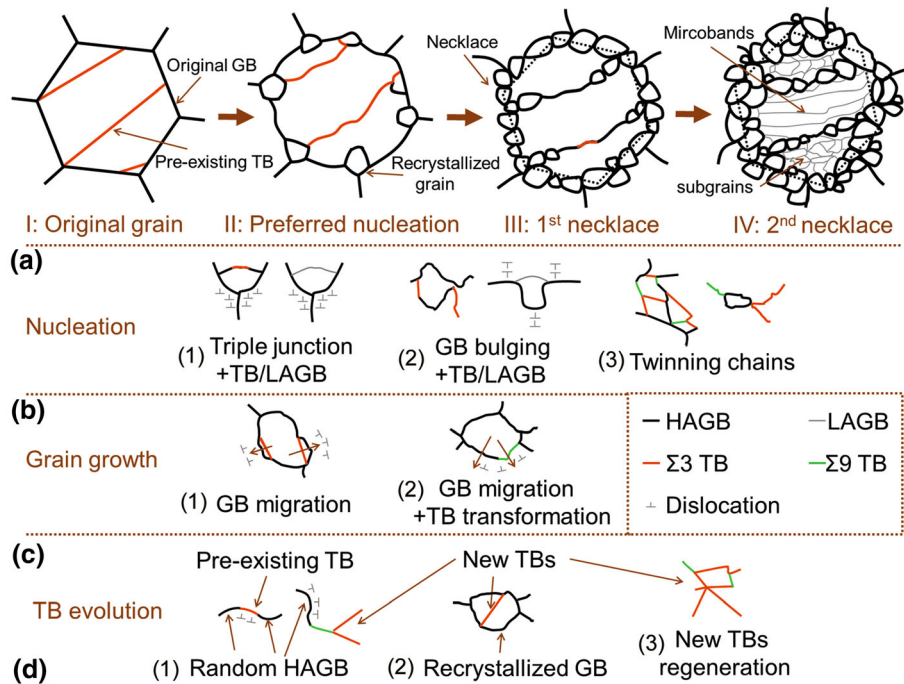


Fig. 11 Schematic representation of the DDRX mechanism in the Incoloy 825 during hot deformation: (a) microstructural evolution (I) shows the original grain with numerous pre-existing TBs, (II) preferred nucleation occurs at triple junctions, (III) first necklace structure forms along the original GB, and (IV) second layer of recrystallized grains are produced accompanied by well-developed subgrains and/or microbands. (b) Nuclei generate (1) at triple junctions and (2) bulging of GBs assisted by the pre-existing TBs and LAGBs and by (3) twinning chains at the front of recrystallization. (c) Grain growth (1) promoted by the formation of TBs and (2) accompanied by the transformation of TBs. (d) Twin boundary evolution including (1) the conversion of pre-existing and newly formed TBs into random HAGBs, (2) the formation of TBs in recrystallized grains, and (3) the regeneration of new TBs

with exponents of -1 and -2 . Given a similar relationship between the driving force and the steady-state D_{DDRX} (Ref 49), the effect of TB during DDRX is enhanced by increasing the driving force, thus resulting in a decreased D_{DDRX} .

5. Conclusions

The DDRX mechanism and evolution of TBs of Incoloy 825 were studied in compression tests in the temperature range from 1050–1200 °C and strain rate range from 0.001–1 s⁻¹. The main results can be summarized as follows:

1. For the multilayered nucleation mechanism in DDRX, the first layer of recrystallized grains forms at the triple junctions and protrusions of original grains; similarly, the main nucleation sites for the following layer include the triple junctions between the new and deformed grains and the bulging HAGBs developed by the transformation

of pre-existing TBs. In addition, the process of twinning chains partly transforming into random HAGBs at the front of the recrystallization zone is another nucleation mechanism for the subsequent recrystallized grains.

2. The pre-existing TBs in the initial grains assist the nucleation by separating the expanding crystals from the deformed grains and then divide the deformed grains into several parts. However, the newly formed straight TBs in the recrystallized grains accelerate the grain growth during DDRX through an increase in misorientation angle, and twinning chains at the front of the recrystallization zone partly convert into random HAGBs to promote nucleation in the next layer.
3. The average number and length of TBs per recrystallized area, i.e., ρ_N and ρ_L , respectively, decrease with increasing temperature and strain and decreasing strain rate, and then they are approximately inversely proportional to the recrystallized grain size (D_{DDRX}) and the square of recrystallized grain size (D_{DDRX}^2), respectively.

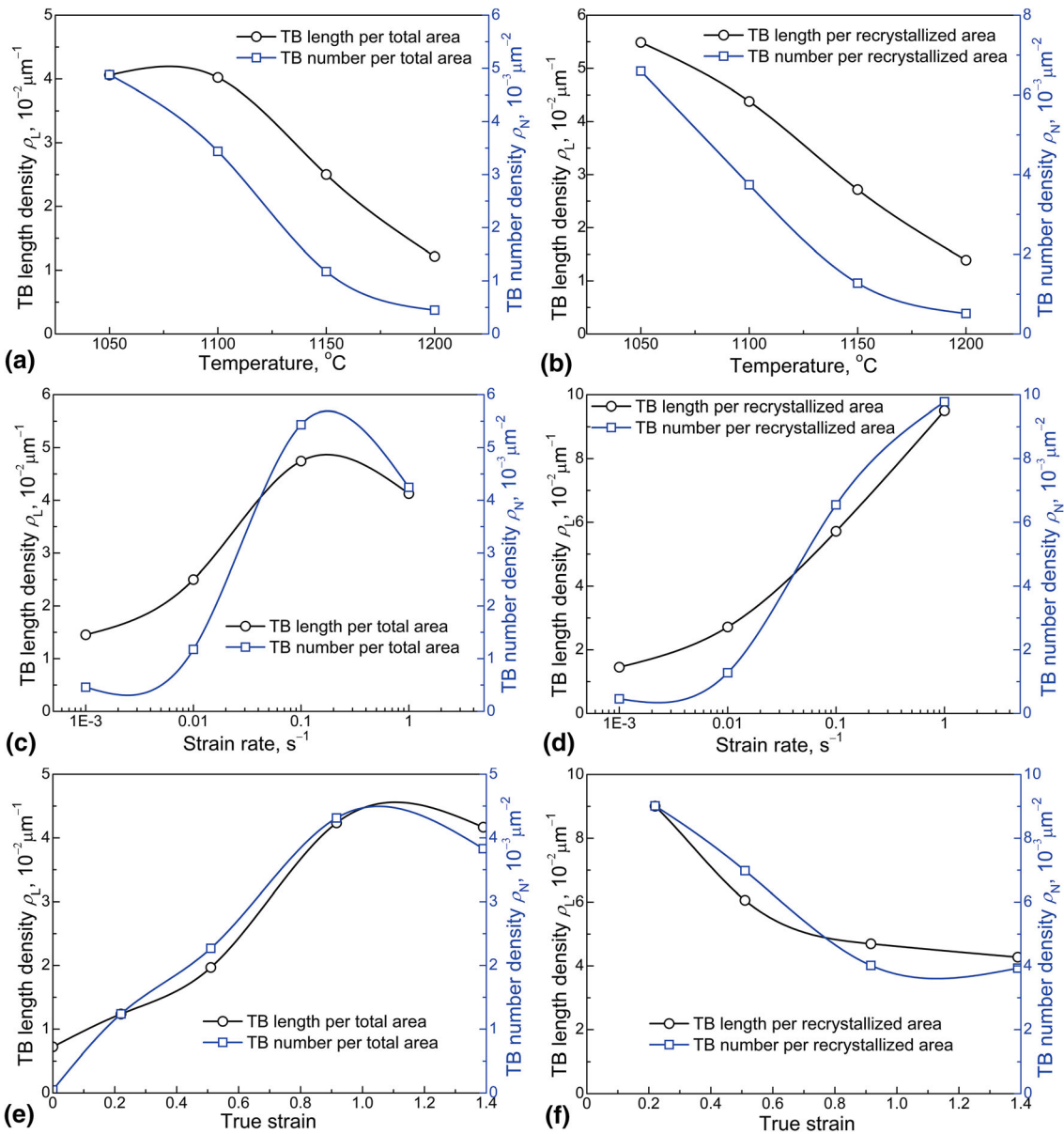


Fig. 12 Evolution of TB density in the total/recrystallized area in the Incoloy 825 under different deformation conditions: (a)(b) different T at $\dot{\epsilon} = 0.01 \text{ s}^{-1}$ and $\epsilon = 0.916$; (c)(d) different $\dot{\epsilon}$ at $T = 1150 \text{ }^\circ\text{C}$ and $\epsilon = 0.916$; and (e)(f) different ϵ under $T = 1100 \text{ }^\circ\text{C}$ and $\dot{\epsilon} = 0.01 \text{ s}^{-1}$

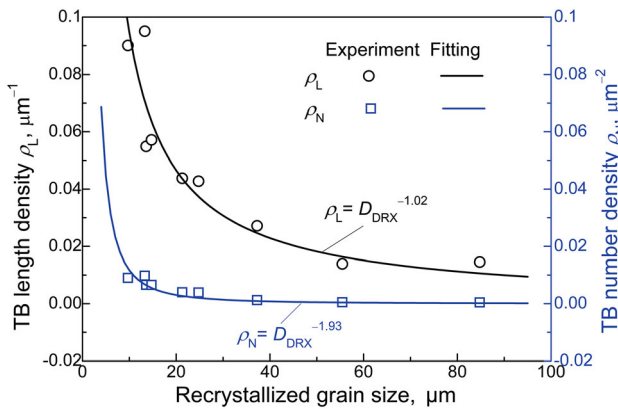


Fig. 13 Relationship between TB densities (ρ_L , ρ_N) in the recrystallized area and recrystallized grain size (D_{DRX}) in the Incoloy 825

Acknowledgments

This work was supported by the National Key R&D Program of China (Grant Numbers 2017YFB0703001, 2017YFB0305100); the Natural Science Foundation of China (Grant Numbers 51790481, 51901185); the Fundamental Research Funds for the Central Universities (Grant Number 3102017jc01002); and the Natural Science Foundation of Shaanxi Province (Grant Number 2020JQ-153). We would like to thank the Analytical & Testing Center of Northwestern Polytechnical University for EBSD and TEM experiments.

References

1. F.J. Humphreys and M. Hatherly, *Recrystallization and Related Annealing Phenomena*, 3rd ed., Pergamon Press, Oxford, 2017

2. T. Sakai, A. Belyakov, R. Kaibyshev, H. Miura, and J.J. Jonas, Dynamic and Post-Dynamic Recrystallization Under Hot, Cold and Severe Plastic Deformation Conditions, *Prog. Mater. Sci.*, 2014, **60**, p 130–207
3. T. Sakai and J.J. Jonas, Dynamic Recrystallization: Mechanical And Microstructural Considerations, *Acta Metall.*, 1984, **32**, p 189–209
4. J.J. Jonas, C.M. Sellars, and W.J. McG. Tegart, Strength and Structure Under Hot-Working Conditions, *Metall. Rev.*, 1969, **14**, p 1–24
5. R.D. Doherty, D.A. Hughes, F.J. Humphreys, J.J. Jonas, D.J. Jensen, M.E. Kassner, W.E. King, T.R. McNelley, H.J. McQueen, and A.D. Rollett, Current Issues in Recrystallization: A Review, *Mater. Sci. Eng., A*, 1997, **238**, p 219–274
6. K. Huang and R.E. Logé, A Review of Dynamic Recrystallization Phenomena in Metallic Materials, *Mater. Des.*, 2016, **111**, p 548–574
7. K. Huang, K. Marthinsen, Q.L. Zhao, and R.E. Logé, The Double-Edge Effect of Second-Phase Particles on the Recrystallization Behaviour and Associated Mechanical Properties of Metallic Materials, *Prog. Mater. Sci.*, 2018, **92**, p 284–359
8. Y. Zhang, N.R. Tao, and K. Lu, Effects of Stacking Fault Energy, Strain Rate and Temperature on Microstructure and Strength of Nanostructured Cu–Al Alloys Subjected to Plastic Deformation, *Acta Mater.*, 2011, **59**, p 6048–6058
9. F.I. Grace and M.C. Inman, Influence of Stacking Fault Energy on Dislocation Configurations in Shock-Deformed Metals, *Metallography*, 1970, **3**(1), p 89–98
10. D. Ponge and G. Gottstein, Necklace Formation During Dynamic Recrystallization: Mechanisms and Impact on Flow Behavior, *Acta Mater.*, 1998, **46**, p 69–88
11. D.F. Li, Q.M. Guo, S.L. Guo, H.J. Peng, and Z.G. Wu, The Microstructure Evolution and Nucleation Mechanisms of Dynamic Recrystallization in Hot-Deformed Inconel 625 Superalloy, *Mater. Des.*, 2011, **32**, p 696–705
12. B. Wang, S.H. Zhang, M. Cheng, and H.W. Song, Dynamic Recrystallization Mechanism of Inconel 690 Superalloy During Hot deformation at High Strain Rate, *J. Mater. Eng. Perform.*, 2013, **22**, p 2382–2388
13. N. Dudova, A. Belyakov, T. Sakai, and R. Kaibyshev, Dynamic Recrystallization Mechanisms Operating in a Ni–20% Cr Alloy Under Hot-to-Warm Working, *Acta Mater.*, 2010, **58**, p 3624–3632
14. A. Chaudhuri, A. Sarkar, R. Kapoor, J.K. Chakravarty, R.K. Ray, and S. Suwas, Understanding the Mechanism of Dynamic Recrystallization During High-Temperature Deformation in Nb-1Zr-0.1C alloy, *J. Mater. Eng. Perform.*, 2019, **28**, p 448–462
15. X.T. Zhong, L. Wang, and F. Liu, Study on Formation Mechanism of Necklace Structure in Discontinuous Dynamic Recrystallization of Incoloy 028, *Acta Metall. Sin.*, 2018, **54**(7), p 969–980
16. H. Miura, T. Sakai, S. Andiarwanto, and J.J. Jonas, Nucleation of dynamic Recrystallization at Triple Junctions in Polycrystalline Copper, *Philos. Mag.*, 2005, **85**(23), p 2653–2669
17. S.Q. Zhu, H.G. Yan, X.Z. Liao, S.J. Moody, G. Sha, Y.Z. Wu, and S.P. Ringer, Mechanisms for Enhanced Plasticity in Magnesium Alloys, *Acta Mater.*, 2015, **82**, p 344–355
18. M. Azarbaras, M. Aghaie-Khafri, A.M. Cabrera, and J. Calvo, Dynamic Recrystallization Mechanisms and Twinning Evolution During Hot Deformation of Inconel 718, *Mater. Sci. Eng. A*, 2016, **678**, p 137–152
19. A. Belyakov, H. Miura, and T. Sakai, Dynamic Recrystallization Under Warm Deformation of Polycrystalline Copper, *ISIJ Int.*, 1998, **38**, p 595–601
20. H. Miura, T. Sakai, R. Mogawa, and J.J. Jonas, Nucleation of Dynamic Recrystallization and Variant Selection in Copper Bicrystals, *Philos. Mag.*, 2007, **87**, p 4197–4209
21. A.M. Wusatowska-Sarneck, H. Miura, and T. Sakai, Nucleation and Microtexture Development Under Dynamic Recrystallization of Copper, *Mater. Sci. Eng. A*, 2002, **323**, p 177–186
22. H. Miura, T. Sakai, R. Mogawa, and G. Gottstein, Nucleation of Dynamic Recrystallization at Grain Boundaries in Copper Bicrystals, *Scr. Mater.*, 2004, **51**, p 671–675
23. H. Beladi, P. Cizek, and P.D. Hodgson, Dynamic Recrystallization of Austenite in Ni–30 pct Fe Model Alloy Microstructure and Texture Evolution, *Metall. Mater. Trans. A*, 2009, **40**, p 1175–1189
24. E. Brunger, X. Wang, and G. Gottstein, Nucleation Mechanisms of Dynamic Recrystallization in Austenitic Steel Alloy 800H, *Scr. Mater.*, 1998, **38**(12), p 1843–1849
25. S. Mandal, A.K. Bhaduri, and V.S. Sarma, Role of Twinning on Dynamic Recrystallization and Microstructure During Moderate to High Strain Rate Hot Deformation of a Ti-Modified Austenitic Stainless Steel, *Metall. Mater. Trans. A*, 2012, **43**, p 2056–2068
26. D.G. Cram, H.S. Zurob, Y.J.M. Brechet, and C.R. Hutchinson, Modelling Discontinuous Dynamic Recrystallization Using a Physically Based Model for Nucleation, *Acta Mater.*, 2009, **57**, p 5218–5228
27. R. Ding and Z.X. Guo, Coupled Quantitative Simulation of Microstructural Evolution and Plastic Flow During Dynamic Recrystallization, *Acta Mater.*, 2001, **49**, p 3163–3175
28. C. Sommitsch and W. Mitter, On Modelling of Dynamic Recrystallization of FCC Materials with Low Stacking Fault Energy, *Acta Mater.*, 2006, **54**, p 357–375
29. P. Bernard, S. Bag, K. Huang, and R.E. Loge, A Two-Site Mean Field Model of Discontinuous Dynamic Recrystallization, *Mater. Sci. Eng. A*, 2011, **528**, p 7357–7367
30. G.B. Shan, Y.Z. Chen, Y.J. Li, C.Y. Zhang, H. Dong, Y.B. Cong, W.X. Zhang, L.K. Huang, and F. Liu, High Temperature Creep Resistance of a Thermally Stable Nanocrystalline Fe-5 at.%, *Scr. Mater.*, 2020, **179**, p 1–5
31. A. Momeni, G.R. Ebrahimi, M. Jahazi, and P. Bocher, Microstructure Evolution at the Onset of Discontinuous Dynamic Recrystallization: A Physics-Based Model of Sub-Grain Critical Size, *J. Alloys Compd.*, 2014, **587**, p 199–210
32. O. Beltran, K. Huang, and R.E. Logé, A Mean Field Model of Dynamic and Post-Dynamic Recrystallization Predicting kinetics, Grain Size and Flow Stress, *Comput. Mater. Sci.*, 2015, **102**, p 293–303
33. Y. Huang and F.J. Humphreys, Measurements of Grain Boundary Mobility During Recrystallization of a Single-Phase Aluminum Alloy, *Acta Mater.*, 1999, **47**, p 2259–2268
34. G. Gottstein, D.A. Molodov, L.S. Shvindlerman, D.J. Srolovitz, and M. Winking, Grain Boundary Migration: Misorientation Dependence, *Curr. Opin. Solid State Mater. Sci.*, 2001, **5**, p 9–14
35. V. Randle, Twinning-Related Grain Boundary Engineering, *Acta Mater.*, 2004, **52**, p 4067–4081
36. H. Jiang, J.X. Dong, M.C. Zhang, and Z.H. Yao, Evolution of Twins and Substructures During Low Strain Rate Hot Deformation and Contribution to Dynamic Recrystallization in Alloy 617B, *Mater. Sci. Eng. A*, 2016, **649**, p 369–381
37. F.C. Liu and T.W. Nelson, Twinning and Dynamic Recrystallization in Austenitic Alloy 718 During Friction Welding, *Mater. Charact.*, 2018, **140**, p 39–44
38. D.P. Field, L.T. Bradford, M.M. Nowell, and T.M. Lillo, The Role of Annealing Twins During Recrystallization of Cu, *Acta Mater.*, 2007, **55**(12), p 4233–4241
39. G.R. Ebrahimi, A. Momeni, H.R. Ezatpour, M. Jahazid, and P. Bocherd, Dynamic Recrystallization in Monel400 Ni–Cu Alloy: Mechanism and Role of Twinning, *Mater. Sci. Eng. A*, 2019, **744**, p 376–385
40. D.G. Brandon, The Structure of High-Angle Grain Boundaries, *Acta Metall.*, 1966, **14**(11), p 1479–1484
41. G. Laplanche, A. Kostka, O.M. Horst, G. Eggeler, and E.P. George, Microstructure Evolution and Critical Stress for Twinning in the CrMnFeCoNi High-Entropy Alloy, *Acta Mater.*, 2016, **118**, p 152–163
42. S. Sahu, P.C. Yadav, and S. Shekhar, Use of Hot Rolling for Generating Low Deviation Twins and a Disconnected Random Boundary Network in Inconel 600 Alloy, *Metall. Mater. Trans. A*, 2018, **49**, p 628–643
43. X.T. Zhong, L. Wang, L.K. Huang, and F. Liu, Transition of Dynamic Recrystallization Mechanism During Hot Deformation of Incoloy 028 Alloy, *J. Mater. Sci. Technol.*, 2020, **42**, p 241–253
44. L. Wang, F. Liu, Q. Zuo, J.J. Cheng, and C.F. Chen, Processing Map and Mechanism of Hot Deformation of a Corrosion-Resistant Nickel-Based Alloy, *J. Mater. Eng. Perform.*, 2017, **26**, p 392–406
45. C.S. Pande, M.A. Imam, and B.B. Rath, Study of Annealing Twins in FCC Metals and Alloys, *Metall. Trans. A*, 1990, **21**(11), p 2891–2896
46. N. Bozzolo, N. Souai, and R.E. Logé, Evolution of Microstructure and Twin Density During Thermomechanical Processing in a γ - γ' Nickel-Based Superalloy, *Acta Mater.*, 2012, **60**(13–14), p 5056–5066
47. Y. Jin, B. Lin, M. Bernacki, G.S. Rohrer, A.D. Rollett, and N. Bozzolo, Annealing Twin Development During Recrystallization and Grain Growth in Pure Nickel, *Mater. Sci. Eng., A*, 2014, **597**, p 295–303
48. Z.G. Li, L.T. Zhang, N.R. Sun, Y.L. Sun, and A.D. Shan, Effects of Prior Deformation and Annealing Process on Microstructure and

Annealing Twin Density in a Nickel-Based Alloy, *Mater. Charact.*, 2014, **95**, p 299–306

49. X.T. Zhong, L.K. Huang, L. Wang, and F. Liu, A Discontinuous Dynamic Recrystallization Model Incorporating the Characteristics of Initial Microstructure, *T. Nonferr. Metal. Soc.*, 2018, **28**, p 2294–2306

Publisher's Note Springer Nature remains neutral with regard to jurisdictional claims in published maps and institutional affiliations.